RSC Advances

PAPER

View Article Online
View Journal | View Issue

Cite this: *RSC Adv.*, 2026, **16**, 25819

Development of coumarin-sulfonate scaffolds for cholinesterase inhibition: experimental and computational studies toward Alzheimer's disease therapy

Ehsan Ullah Mughal, *[a] Nafeesa Naeem, [a] Aneela Shaheen Cheema,[a] Gehan Ahmed Othman,[b] Amina Sadiq,[c] Songül Bayrak,[d] Namık Kılınç,[e] Mohammed B. Hawsawi, [f] Sobhi M. Gomha [g] and Züleyha Almaz*[h]

The development of effective cholinesterase inhibitors remains a key strategy for the symptomatic management of Alzheimer's disease (AD); however, the identification of structurally versatile scaffolds capable of dual AChE/BChE inhibition remains limited. In this context, coumarin–sulfonate hybrids offer a promising framework for exploring structure–activity relationships due to their tunable electronic and steric properties. In the present study, a series of nine coumarin–sulfonate derivatives (**1–9**) were synthesized *via* a two-step procedure and evaluated for their inhibitory activity against acetylcholinesterase (AChE) and butyrylcholinesterase (BChE) using Ellman's assay. Among the tested compounds, derivative **3** (2,4,6-trimethylphenyl sulfonate) exhibited the highest inhibitory activity with IC_{50} values of 6.476 nM for AChE and 11.948 nM for BChE, indicating potent dual inhibition. Compound **2** also showed strong dual activity, whereas compound **5** displayed relatively higher selectivity toward BChE. Structure–activity relationship (SAR) analysis revealed that both electronic properties and steric bulk of the aryl sulfonate substituents significantly influenced enzyme inhibition. In addition, computational studies were performed to provide qualitative insights into ligand–enzyme interactions, supporting the experimentally observed activity trends. Overall, the results highlight coumarin–sulfonate derivatives as promising scaffolds for cholinesterase inhibition and provide a basis for further structural optimization toward AD-related targets.

Received 27th March 2026
Accepted 8th May 2026

DOI: 10.1039/d6ra02535h

rsc.li/rsc-advances

1. Introduction

Alzheimer's disease (AD) is a chronic neurodegenerative disorder that involves a slow and gradual decline, causing dementia in the elderly, affecting millions of lives around the world.[1] AD is clinically characterized by progressive memory and cognitive impairment, which are usually followed by neuropsychiatric symptoms. The molecular hallmarks of the disease are characterized by the accumulation of extracellular amyloid-β aggregates and the intracellular formation of neurofibrillary tangles composed of hyperphosphorylated tau protein, both of which contribute to synaptic dysfunction and neuronal loss.[2,3] Moreover, despite huge research efforts, AD is regarded as a multifactorial disease determined by genetic, biochemical, and environmental factors; effective disease-modifying treatments are not available. The significance of such an approach is underscored by the focus on enzymes and their inhibitors as potential therapeutic avenues for addressing cholinergic deficits and cognitive dysfunction in AD.[4] One of the first and most influential hypotheses to explain Alzheimer's disease (AD) pathophysiology is the cholinergic hypothesis, which associates cognitive impairment with an impairment in cholinergic neurotransmission in the brain. This is substantiated by data documenting an impaired acetylcholine release, together with changes in cholinesterase activity performed at critical areas for learning and memory.[5,6] Acetylcholine is metabolized by two similar enzymes, acetylcholinesterase (AChE) and butyrylcholinesterase (BChE), that are distinct from

[a]*Department of Chemistry, University of Gujrat, Gujrat-50700, Pakistan. E-mail: ehsan.ullah@uog.edu.pk*

[b]*Biology Department, College of Science, King Khalid University, Abha, 61421, Saudi Arabia*

[c]*Department of Chemistry, Govt. College Women University, Sialkot-51300, Pakistan*

[d]*Department of Chemistry, Faculty of Science, Ataturk University, Erzurum, 25240, Turkey*

[e]*Department of Medical Services and Techniques, Vocational School of Health Services, Igdir University, Igdir, 76000, Turkey*

[f]*Department of Chemistry, Faculty of Science, Umm Al-Qura University, Makkah 21955, Saudi Arabia*

[g]*Chemistry Department, Faculty of Science, Islamic University of Madinah, Madinah, 42351, Saudi Arabia*

[h]*Department of Molecular Biology and Genetics, Faculty of Arts and Sciences, Mus Alparslan University, Mus, 49250, Turkey. E-mail: z.turkoglu@alparslan.edu.tr*

one another in their tissue distribution and their role in the regulation of neurotransmitters.[7–9] In the normal brain, the majority of acetylcholine hydrolysis is mediated by AChE. At the same time, the role of BChE is secondary, but during the progression of the disease, the activity of AChE is significantly reduced. In contrast, the activity of BChE is increased, thereby emphasizing the role of both enzymes in the pathology of AD.[10,11]

Clinically used cholinesterase inhibitors increase synaptic acetylcholine levels and remain the main symptomatic therapy for mild to moderate AD. Although these medications are effective, their efficacy is variable and transient, depending on the progression of the disease, while their adverse effects are another factor that limits their use. Tacrine, which was the first dual inhibitor of AChE and BChE to be developed as an AD treatment, provided proof of concept for cholinergic enhancement but was withdrawn from use owing to toxicity, paving the way for safer agents to be developed.[12–14] Although significant progress has been made in developing treatments for AD, these treatments do not stop the progression of the disease, which confirms the necessity to continue developing new cholinesterase inhibitors, particularly dual inhibitors of AChE and BChE.

Recent advances in medicinal chemistry have emphasized the importance of sulfonate-containing scaffolds as promising structural motifs for the development of cholinesterase inhibitors for Alzheimer's disease therapy.[15–17] The introduction of sulfonate functionalities can enhance enzyme–ligand interactions through hydrogen bonding, electrostatic interactions, and improved physicochemical properties, facilitating binding within the catalytic gorge of AChE and BChE. Several recent studies have reported the synthesis and biological evaluation of diverse sulfonate-based derivatives, including naphthalene-2-sulfonate thiosemicarbazones,[18] barbiturate–sulfonate conjugates,[19] quinoline-8-sulfonates,[20] Schiff base sulfonates,[21] hydrazone-sulfonate[22] and aurone sulfonate derivatives,[23] which demonstrated significant inhibitory activity against cholinesterases, in some cases exhibiting micromolar to nanomolar potency (Fig. 1). In addition to enzyme inhibition, molecular docking studies confirmed favorable interactions with key residues in the catalytic active sites, while certain compounds also displayed multifunctional properties such as carbonic anhydrase inhibition, neuroprotective effects, and modulation of oxidative stress-related pathways.[24,25] Collectively, these findings highlight the growing interest in sulfonate-containing frameworks as versatile pharmacophores in anti-Alzheimer drug discovery, supporting their incorporation into bioactive scaffolds for the development of novel and more effective dual cholinesterase inhibitors.

Coumarins (Fig. 2) have been recognized as a promising lead structure in the search for cholinesterase inhibitors owing to their flexibility, good physicochemical properties, and capacity to incorporate a wide variety of substituents that modulate the activity of AChE and BChE.

Previous studies have shown that when appropriately substituted, coumarin derivatives can interact effectively with critical regions of cholinesterases, hence showing considerable inhibitory activity.[26,27] Additionally, coumarin sulfonate derivatives have emerged as promising candidates in medicinal chemistry due to their favorable structural versatility and ability to interact with multiple biological targets.[28–32] The presence of sulfonate moiety can enhance binding interactions within enzyme active sites through hydrogen bonding and electrostatic effects, thereby improving inhibitory activity against cholinesterases. Despite the growing interest in both coumarin-based and sulfonate-containing cholinesterase inhibitors, the systematic exploration of aryl sulfonate substitution on the coumarin scaffold remains limited. In particular, the influence of electronic and steric variations within the sulfonate moiety on dual AChE/BChE inhibition has not been comprehensively investigated. In this context, the present study was designed to develop a focused series of coumarin–sulfonate derivatives bearing diverse aryl substituents with varying electronic characteristics (electron-donating and electron-withdrawing groups) and substitution patterns. This design enables a preliminary SAR assessment aimed at identifying key structural features governing enzyme inhibition. Accordingly, a set of nine coumarin–sulfonate derivatives was synthesized and evaluated for their inhibitory activity against AChE and BChE using the Ellman assay. In addition, computational studies were performed to provide a qualitative interpretation of ligand–enzyme interactions. The overall objective of this work is to explore coumarin–sulfonate scaffolds as potential cholinesterase inhibitors and to generate insights that may guide future optimization, rather than to establish definitive therapeutic candidates.

2. Experimental section

2.1. General procedure for the synthesis of coumarin–sulfonate esters

In step I, the concentrated sulfuric acid (98%, 100 mL) was cooled to 10 °C in a reaction vessel. *m*-Dihydroxybenzene (10.0 g, 90.8 mmol) was dissolved in ethyl acetoacetate (13.0 mL, 102.7 mmol) to form a homogeneous solution. This solution was added dropwise to the cooled sulfuric acid under continuous stirring. After the addition was complete, the reaction mixture was stirred at room temperature for 16 h. Upon completion, the mixture was poured into ice-cold water with stirring and allowed to stand overnight. The resulting solid was collected by filtration and washed thoroughly with water. The crude product was dissolved in 5% sodium hydroxide solution and filtered to remove insoluble impurities. The filtrate was then acidified with 10% sulfuric acid until the pH dropped below 6. The precipitated product was collected by filtration, washed with cold water, and dried to yield white needle-shaped crystals of 4-methyl-7-hydroxycoumarin.[33]

In step-II, 4-methyl-7-hydroxycoumarin (1.00 g, 5.32 mmol) was dissolved in dry dichloromethane (20 mL) under stirring. Triethylamine (0.75 mL, 5.37 mmol) was added dropwise to the solution as a base. The reaction mixture was cooled to 0–5 °C using an ice bath to maintain a low temperature. After stirring for 30 min under cooling, a solution of the appropriate aryl sulfonyl chloride (1.17 g, 5.85 mmol) in dry dichloromethane

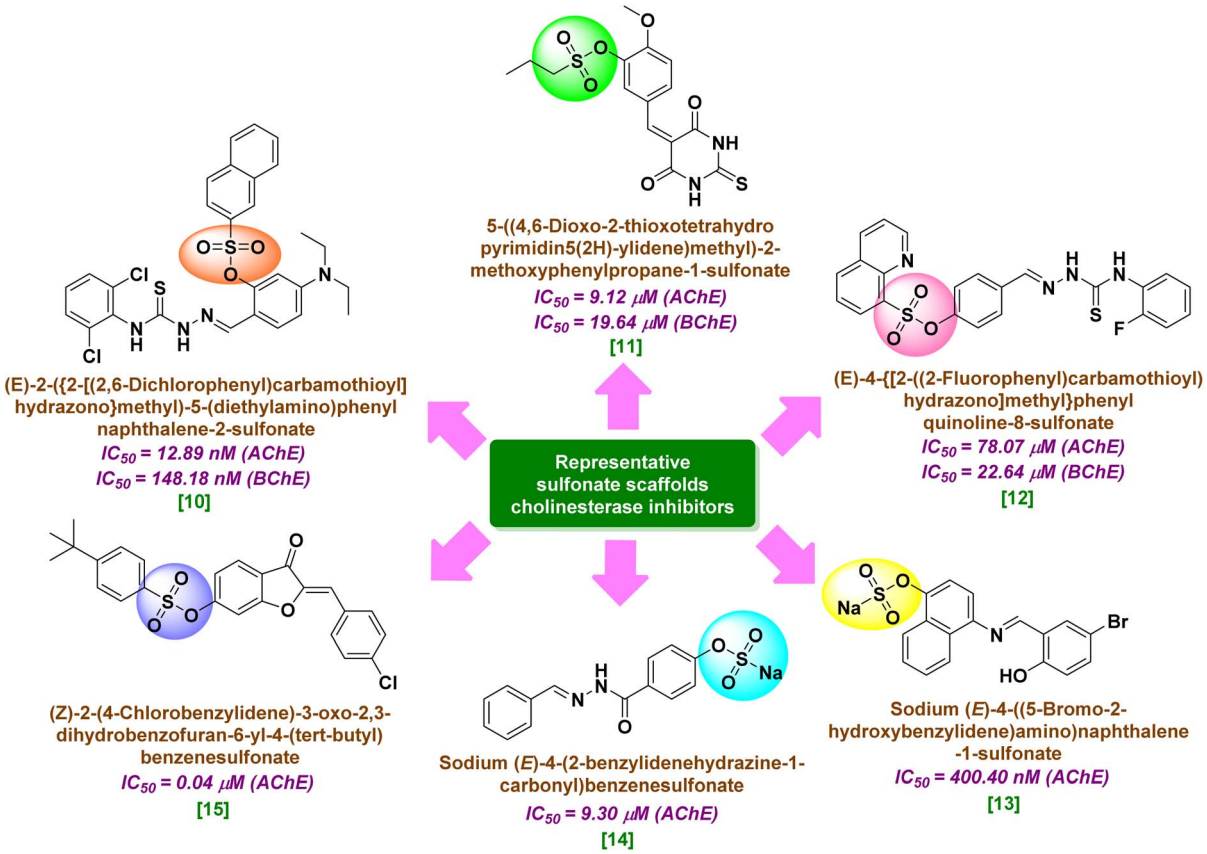

Fig. 1 Representative sulfonate scaffolds of cholinesterase inhibitors reported in the literature.

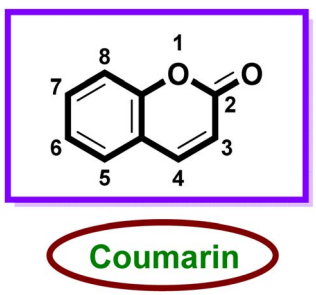

Fig. 2 General structure of coumarin scaffold.

(10 mL) was added dropwise while maintaining the low temperature. Following the addition, the reaction mixture was allowed to gradually warm to room temperature and stirred until the progress of the reaction was confirmed complete by thin-layer chromatography (TLC). Upon completion, the reaction mixture was extracted with dichloromethane (3 × 20 mL), and the combined organic layers were washed three times with saturated saline solution to remove residual water-soluble impurities. The organic layer was dried over anhydrous sodium sulfate and filtered. Solvent removal under reduced pressure yielded crude sulfonated coumarin. The crude product was purified by recrystallization from methanol to afford the desired coumarin sulfonate ester derivatives as pure crystalline solids.[28]

2.2. Determination of AChE and BChE inhibitory activity

Inhibitory activities of the prepared compounds on AChE and BChE were determined by the modified spectrophotometric method according to Ellman's assay.[13,34–39] This approach is based on the follow-up of the reduction of 5-mercapto-2-nitrobenzoic acid yielded by the interaction between thiocholine produced in enzymatic hydrolysis and 5,5′dithiobis (2-nitrobenzoic acid) (DTNB). Acetylthiocholine iodide and butyrylthiocholine iodide were utilized as eeAChE (electric eel AChE) and eqBChE (equine serum BChE) substrates, respectively. The stock solutions of the test compounds were made into 1 mg mL^{-1} in dimethyl sulfoxide (DMSO) and further diluted with ultrapure water to the required concentrations. For the inhibition assay, the enzyme solution was incubated with different concentrations of the inhibitor in buffer (Tris–HCl buffer, pH 8.0 for AChE; phosphate buffer for BChE) and incubated at room temperature for 5 min. DTNB solution was added, and after that, the rate of the appropriate substrate initiated the enzymatic reaction. The reaction mixture was incubated, and the change in absorbance at 412 nm was measured with a microplate spectrophotometer within 5 minutes after starting the reaction. Activity in the absence of inhibitors was taken as 100% activity (control). Percent

inhibition values were calculated relative to this control, and researchers created inhibition curves by plotting remaining enzyme activity against different levels of inhibitor concentration. The plots were used to determine the IC_{50} values, which showed the inhibitor concentrations needed to decrease enzyme activity by half. Tacrine served as the reference inhibitor for the experiments, which were conducted under the same testing conditions.

2.3. *In silico* investigations

2.3.1 Induced-fit molecular docking. The study employed complete computational methods to determine binding pocket dimensions for AChE and BChE enzymes, which showed affinity to coumarin derivatives through the induced-fit molecular docking (IFD) method developed by Sherman and his team from their study published in 2018.[40] This approach was developed following methodologies reported elsewhere.[41–47] The docking studies were conducted with Maestro 13.9 in the Schrödinger Molecular Modeling Suite.[48] The 3D crystal structures of AChE (PDB ID: 4TVK) and BChE (PDB ID: 4TPK) were obtained from the RCSB Protein Data Bank. Both protein structures were prepared with the Protein Preparation Wizard,[49] before docking, which involved adding missing hydrogen atoms and setting protonation states to their physiological pH values and correcting structural errors. The OPLS4 force field was used to conduct post-optimization and restrained energy minimization, which helped them achieve extremely low energy states. This established docking grids by centering the grid box on co-crystallized ligands of enzyme active sites, which identified docking regions. The LigPrep module created ligand structures by generating proper ionization states at pH 7.0 $\pm$ 2.0, which correctly simulated physiological conditions for docking simulations.

2.3.2 MM-GBSA binding free energy calculations. The binding free energy values for protein-ligand complexes were determined through MM-GBSA calculations, which used ΔG_{bind} as the binding free energy measurement. The system uses molecular mechanics energy calculations together with implicit solvation models to determine the strength of ligand-receptor binding. The calculations used the Prime/MM-GBSA module from the Schrödinger suite, which applied the OPLS4 force field and VSGB solvation model to evaluate solvation effects.[50,51] The analyses provided a method to compare the energetic stability of docked complexes, which included both AChE and BChE enzymes.

2.3.3 Molecular dynamics simulations. The Molecular Dynamics (MD) simulations were used to investigate the time-dependent stability and dynamic behavior of the most promising protein-ligand complex using D. E. Shaw's Desmond simulation package.[52] The compound was finally chosen for an in-depth dynamic investigation based on the molecular docking and MM-GBSA results, which had the best affinity towards both targets. The protein–ligand complex was built by the Desmond system builder and then located in an orthorhombic simulation box, with a minimum distance of 10 Å from the complex to the box edge. The system was solvated in the TIP3P water model and neutralized with Na^+ and Cl^- ions to approximate a physiological salt concentration of 0.15 M. Subsequent energy minimization was performed with the OPLS4 force field to remove unfavorable contacts and stabilize the system for production runs. After that, a 250 ns MD simulation was carried out under constant temperature (300 K) and pressure (1 bar) conditions with standard Desmond protocols. In the simulation, a 2.5 fs time step and RESPA integrator were used in order to save computation time. During the simulation, the protein–ligand interactions were monitored. By calculating the root mean square deviation (RMSD) of the protein backbone Cα atoms and the ligand heavy atoms, the structural stability was assessed, which gave detailed insight into the conformational stability and binding of the ligands during the period of the simulation.

2.3.4 ADME property prediction. In order to evaluate the pharmacokinetic performance and drug-like properties of the selected coumarin derivatives (**1–9**), *in silico* ADME profiling was done. The QikProp module incorporated into Maestro 13.9 was utilized to predict important parameters concerning absorption, distribution, metabolism, and excretion. QikProp predicts various physicochemical and pharmacokinetic properties by benchmarking the candidate compound against the properties of around 95% of the marketed drugs. The evaluation discussed above showed the oral bioavailability, metabolic stability, and drug-likeness of the studied coumarin derivatives.

3. Results and discussion

3.1. Chemistry

4-Methyl-7-hydroxycoumarin was synthesized *via* Pechmann condensation of *m*-dihydroxybenzene with ethyl acetoacetate in the presence of sulfuric acid, followed by purification through alkaline treatment and recrystallization. Sulfonate derivatives were obtained by reacting 4-methyl-7-hydroxycoumarin with appropriate aryl sulfonyl chlorides in dry dichloromethane using triethylamine as a base. The reaction products were isolated by extraction, washed, dried, and purified by recrystallization to afford the corresponding coumarin sulfonate esters as crystalline solids (Scheme 1).

The synthesized coumarin derivative was fully characterized using FTIR, ^{1}H-, and ^{13}C-NMR spectroscopy, and the obtained data are consistent with the proposed structure. The FTIR spectrum displayed a broad absorption band at 3374 cm^{-1}, which is attributed to the O–H stretching vibration. Importantly, this band, along with the strong absorptions observed in the region 1251–1073 cm^{-1}, corresponding to S=O stretching vibrations, clearly indicates the sulfonation of the hydroxyl (–OH) group. The aromatic C–H stretching appeared at 3071 cm^{-1}, while the characteristic lactone carbonyl (C=O) of the coumarin nucleus was observed at 1691 cm^{-1}. Peaks at 1566 and 1457 cm^{-1} are assigned to aromatic C=C stretching vibrations. The band at 1380 cm^{-1} corresponds to methyl bending vibrations, and the absorption at 627 cm^{-1} is due to aromatic C–H out-of-plane bending.

The observed chemical shifts are in good agreement with typical coumarin derivatives. The H-3 proton generally

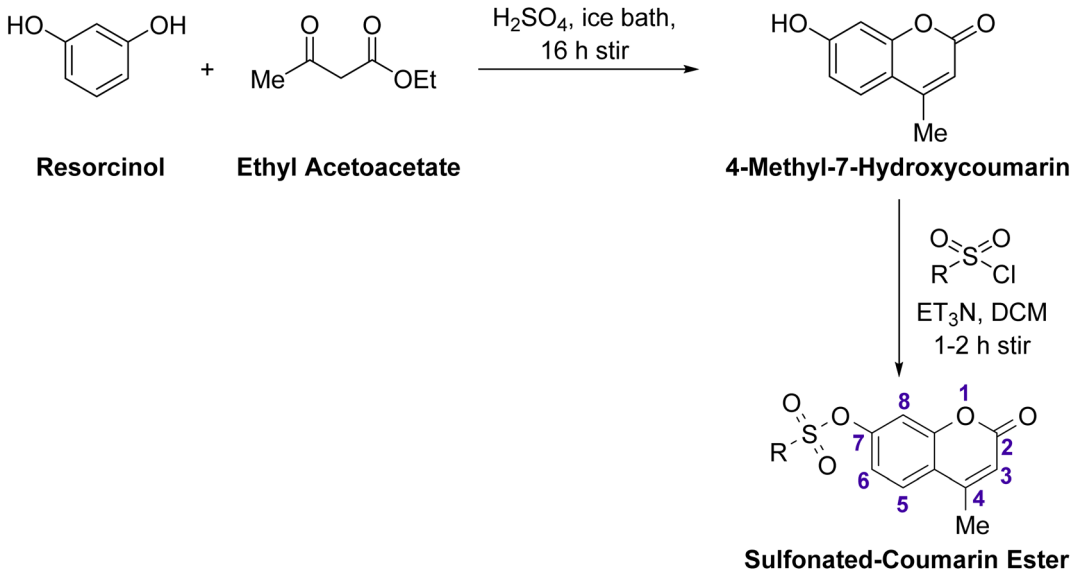

Scheme 1 Synthesis of coumarin-sulfonated esters (**1–9**).

resonates in the range δ 6.0–6.5 ppm as a singlet due to its isolated olefinic nature. The H-5 and H-6 protons typically appear in the range δ 7.0–8.0 ppm, showing *ortho* coupling ($J \approx$ 8–9 Hz), as observed in this study. The H-8 proton usually resonates around δ 6.5–7.2 ppm with a small meta coupling constant ($J \approx$ 2 Hz). The H-7 position, when substituted (as in this case due to sulfonation), does not show a proton signal, further supporting substitution at this site. The ^{13}C-NMR spectrum showed characteristic signals for the coumarin scaffold. The lactone carbonyl carbon (C-2) appeared downfield at δ 159.9 ppm. Oxygenated aromatic carbons (C-4, C-7, and C-8a) were observed in the range δ 151–154 ppm. The remaining aromatic and olefinic carbons resonated between δ 110–134 ppm, consistent with the conjugated coumarin and phenyl systems. The aliphatic methyl carbon was observed upfield at δ 18.7 ppm.

3.1.1 4-Methyl-2-oxo-2*H*-1-benzopyran-7-yl 4-bromobenzene-1-sulfonate (1).

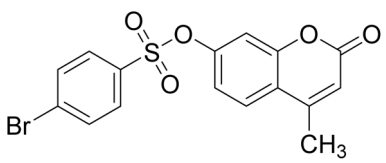

Off white crystalline solid, M. P. 171–173 °C; yield: 77%; FTIR (cm^{-1}): 3374, 3071, 1691, 1566, 1457, 1380, 1251, 1073, 627; ^{1}H NMR (600 MHz, $CDCl_3$) δ 7.76–7.67 (m, 4H, Ar–H), 7.58 (d, J = 8.7 Hz, 1H, Ar–H), 7.08–7.03 (m, 1H, Ar–H), 6.95 (d, J = 2.3 Hz, 1H, Ar–H), 6.30 (s, 1H, H-3), 2.42 (s, 3H, –CH_3); ^{13}C NMR (151 MHz, $CDCl_3$) δ 159.9, 154.0, 151.6, 151.2, 133.9, 132.9, 130.3, 125.9, 119.1, 118.5, 115.3, 110.9, 18.7; accurate mass (ESI) of [M + H]$^+$: calculated for $C_{16}H_{12}BrO_5S$ 394.9588; found 394.9569.

3.1.2 4-Methyl-2-oxo-2*H*-1-benzopyran-7-yl 4-methoxybenzene-1-sulfonate (2).

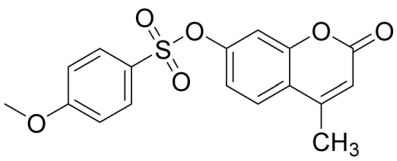

White crystalline solid, M. P. 127–129 °C; yield: 79%; FTIR (cm^{-1}): 3382, 3091, 1700, 1594, 1493, 1372, 1267, 1086, 697; ^{1}H NMR (600 MHz, $CDCl_3$) δ 7.78 (d, J = 8.9 Hz, 2H, Ar–H), 7.57 (d, J = 8.7 Hz, 1H, Ar–H), 7.10 (dd, J = 8.7, 2.3 Hz, 1H, Ar–H), 6.99 (d, J = 8.9 Hz, 2H, Ar–H), 6.86 (d, J = 2.3 Hz, 1H, Ar–H), 6.28 (d, J = 1.4 Hz, 1H, H-3), 3.91 (s, 2H, –OCH_3), 2.42 (d, J = 1.4 Hz, 3H, –CH_3); ^{13}C NMR (151 MHz, $CDCl_3$) δ 164.5, 160.1, 153.9, 151.7, 151.6, 130.8, 126.1, 125.7, 118.9, 118.8, 115.1, 114.6, 111.0, 55.8, 18.7; accurate mass (ESI) of [M + H]$^+$: calculated for $C_{17}H_{15}O_6S$ 347.0589; found 347.0578.

3.1.3 4-Methyl-2-oxo-2*H*-1-benzopyran-7-yl 2,4,6-trimethylbenzene-1-sulfonate (3).[28]

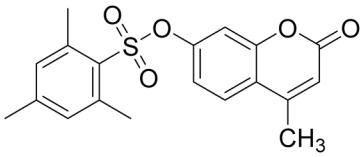

White crystalline solid, M. P. 163–165 °C; yield: 68%; FTIR (cm^{-1}): 3334, 2968, 1731, 1603, 1492, 1364, 1187, 661; ^{1}H NMR (600 MHz, $CDCl_3$) δ 7.56 (d, J = 8.7 Hz, 1H, Ar–H), 7.09 (dd, J = 8.7, 2.3 Hz, 1H, Ar–H), 7.00 (s, 2H, Ar–H), 6.83 (d, J = 2.3 Hz, 1H, Ar–H), 6.26 (s, 1H, H-3), 2.58 (s, 6H, –CH_3-2′,6′), 2.41 (s, 3H, –CH_3-4′), 2.34 (s, 3H, –CH_3-4); ^{13}C NMR (151 MHz, $CDCl_3$) δ 160.2, 153.9, 151.8, 151.6, 144.5, 140.4, 132.1, 130.1, 125.7, 118.8, 118.7, 115.0, 110.6, 22.8, 21.2, 18.7; accurate mass (ESI) of [M + H]$^+$: calculated for $C_{19}H_{19}O_5S$ 359.0953; found 359.0947.

3.1.4 4-Methyl-2-oxo-2*H*-1-benzopyran-7-yl 2,5-dichlorobenzene-1-sulfonate (4).[28]

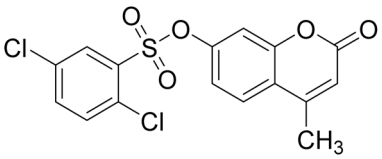

White crystalline solid, M. P. 182–184 °C; yield: 81%; FTIR (cm^{-1}): 3092, 2849, 1701, 1602, 1498, 1380, 1275, 1102, 709; ^1H NMR (600 MHz, $CDCl_3$) δ 7.92 (d, J = 1.2 Hz, 1H, Ar–H), 7.73–7.43 (m, 3H, Ar–H), 7.19 (dd, J = 8.8, 2.4 Hz, 1H, Ar–H), 7.06 (d, J = 2.4 Hz, 1H, Ar–H), 6.28 (d, J = 1.8 Hz, 1H, H-3), 2.41 (d, J = 1.3 Hz, 3H, –CH_3); ^{13}C NMR (151 MHz, $CDCl_3$) δ 160.0, 154.1, 151.7, 151.0, 135.7, 134.5, 133.7, 133.6, 132.2, 131.7, 126.2, 119.4, 118.4, 115.5, 110.8, 18.9; accurate mass (ESI) of $[M + H]^+$: calculated for $C_{16}H_{11}Cl_2O_5S$ 384.9704; found 384.9692.

3.1.5 4-Methyl-2-oxo-2*H*-1-benzopyran-7-yl 4-chlorobenzene-1-sulfonate (5).

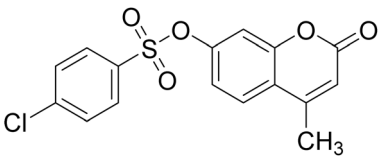

White crystalline solid, M. P. 166–168 °C; yield: 86%; FTIR (cm^{-1}): 3366, 3079, 1721, 1607, 1470, 1372, 1251, 1198, 627; ^1H NMR (600 MHz, $CDCl_3$) δ 7.85–7.76 (m, 2H, Ar–H), 7.58 (d, J = 8.7, 1H, Ar–H), 7.54 (dd, J = 8.7, 1.0 Hz, 2H, Ar–H), 7.06 (dt, J = 8.7, 2.1 Hz, 1H, Ar–H), 6.94 (d, J = 2.1 Hz, 1H, Ar–H), 6.29 (s, 1H, H-3), 2.42 (s, 3H, –CH_3); ^{13}C NMR (151 MHz, $CDCl_3$) δ 159.9, 154.0, 151.6, 151.2, 141.7, 133.4, 129.9, 125.9, 119.1, 118.5, 115.3, 110.9, 18.7; accurate mass (ESI) of $[M + H]^+$: calculated for $C_{16}H_{12}ClO_5S$ 351.0094; found 351.0078.

3.1.6 4-Methyl-2-oxo-2*H*-1-benzopyran-7-yl 2-methylbenzene-1-sulfonate (6).

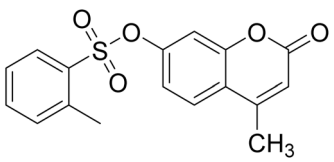

White crystalline solid, M. P. 133–135 °C; yield: 76%; FTIR (cm^{-1}): 3062, 1732, 1605, 1490, 1372, 1056, 699; ^1H NMR (600 MHz, $CDCl_3$) δ 7.83 (dd, J = 8.0, 1.4 Hz, 1H, Ar–H), 7.61–7.51 (m, H-5, 2H, Ar–H), 7.44 (d, J = 7.6 Hz, 1H, Ar–H), 7.34–7.28 (m, 1H, Ar–H), 7.09 (dd, J = 8.7, 2.4 Hz, 1H, Ar–H), 6.87 (d, J = 2.4 Hz, 1H, Ar–H), 6.27 (d, J = 1.4 Hz, 1H, H-3), 2.79 (s, 3H, –CH_3-6′), 2.41 (d, J = 1.4 Hz, 3H, –CH_3-4); ^{13}C NMR (151 MHz, $CDCl_3$) δ 160.1, 153.9, 151.7, 151.5, 138.8, 134.7, 133.7, 132.9, 130.5, 126.5, 125.8, 118.9, 118.6, 115.1, 110.6, 20.5, 18.7; accurate mass (ESI) of $[M + H]^+$: calculated for $C_{17}H_{15}O_5S$ 331.0640; found 331.0629.

3.1.7 4-Methyl-2-oxo-2*H*-1-benzopyran-7-yl 2-chlorobenzene-1-sulfonate (7).

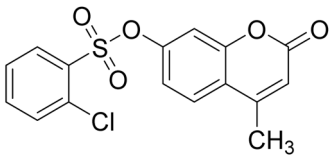

White crystalline solid, M. P. 151–153 °C; yield: 79%; FTIR (cm^{-1}): 3094, 1714, 1608, 1345, 1189, 663; ^1H NMR (600 MHz, $CDCl_3$) δ 7.96 (dd, J = 8.0, 1.6 Hz, 1H, Ar–H), 7.66 (dd, J = 8.0, 1.4 Hz, 1H, Ar–H), 7.65–7.59 (m, 1H, Ar–H), 7.57 (d, J = 8.8 Hz, 1H, Ar–H), 7.43–7.37 (m, 1H, Ar–H), 7.21 (dd, J = 8.8, 2.4 Hz, 1H, Ar–H), 7.05 (d, J = 2.4 Hz, 1H, Ar–H), 6.28 (d, J = 1.3 Hz, 1H, H-3), 2.41 (d, J = 1.3 Hz, 3H, –CH_3); ^{13}C NMR (151 MHz, $CDCl_3$) δ 160.0, 155.0, 151.6, 151.2, 135.6, 133.4, 133.1, 132.4, 127.3, 125.9, 119.1, 118.5, 115.2, 110.7; accurate mass (ESI) of $[M + H]^+$: calculated for $C_{16}H_{12}ClO_5S$ 351.0094; found 351.0086.

3.1.8 4-Methyl-2-oxo-2*H*-1-benzopyran-7-yl naphthalene-2-sulfonate (8).[28]

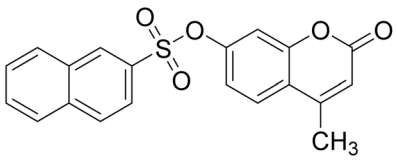

White crystalline solid, M. P. 162–164 °C; yield: 84%; FTIR (cm^{-1}): 3289, 1696, 1525, 1360, 1243, 1162, 627; ^1H NMR (600 MHz, $CDCl_3$) δ 8.42 (d, J = 1.9 Hz, 1H, Ar–H), 8.03 (d, J = 8.8 Hz, 1H, Ar–H), 7.99–7.92 (m, 2H, Ar–H), 7.86 (dd, J = 8.8, 1.9 Hz, 1H, Ar–H), 7.76–7.70 (m, 1H, Ar–H), 7.68–7.61 (m, 1H, Ar–H), 7.53 (d, J = 8.7 Hz, 1H, Ar–H), 7.09 (dd, J = 8.7, 2.3 Hz, 1H, Ar–H), 6.93 (d, J = 2.3 Hz, 1H, Ar–H), 6.25 (d, J = 1.3 Hz, 1H, H-3), 2.39 (d, J = 1.3 Hz, 3H, –CH_3); ^{13}C NMR (151 MHz, $CDCl_3$) δ 160.0, 153.9, 151.6, 151.5, 135.6, 131.7, 131.7, 130.6, 130.0, 129.9, 129.5, 128.2, 128.1, 125.8, 122.6, 118.9, 118.7, 115.2, 111.0, 18.7; accurate mass (ESI) of $[M + H]^+$: calculated for $C_{20}H_{15}O_5S$ 367.0640; found 367.0628.

3.1.9 4-Methyl-2-oxo-2*H*-chromen-7-yl 4-acetamidocyclohexa-2,4-diene-1-sulfonate (9).

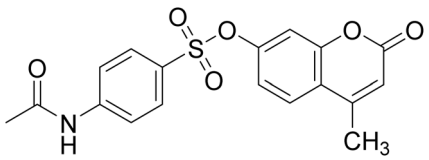

White crystalline solid, M. P. 214–216 °C; yield: 73%; FTIR (cm^{-1}): 3390, 3079, 1696, 1493, 1372, 1275, 1088, 705; ^1H NMR (600 MHz, $CDCl_3$) δ 7.81 (d, J = 8.7 Hz, 2H, Ar–H), 7.74 (d, J = 8.8 Hz, 2H, Ar–H), 7.60 (d, J = 8.7 Hz, 1H, Ar–H), 7.49 (s, 1H, NH), 7.13 (dd, J = 8.7, 2.3 Hz, 1H, Ar–H), 6.86 (d, J = 2.3 Hz, 1H, Ar–H), 6.30 (d, J = 1.5 Hz, 1H, H-3), 2.44 (s, 3H, –$COCH_3$), 2.13 (s, 3H, –CH_3); ^{13}C NMR (151 MHz, $CDCl_3$) δ 168.6, 160.1, 153.8, 151.7, 151.5, 143.6, 130.0, 129.0, 125.7, 119.1, 119.0, 118.8, 115.1, 111.0, 24.8, 18.7; accurate mass (ESI) of $[M + H]^+$: calculated for $C_{18}H_{16}NO_6S$ 374.0698; found 375.0786.

3.2. Cholinesterase inhibitory activities

The nine compounds (**1–9**) showed potent inhibition of AChE and BChE at low nanomolar range. The AChE IC_{50} ranges from 6.476 nM to 53.307 nM, while the BChE IC_{50} ranges from 11.948 nM to 53.307 nM (Table 1). Importantly, there were several analogues (*e.g.* **2**, **3**, and **6**) more potent than the reference inhibitor tacrine against both enzymes. Compound **3** exhibited a balanced dual inhibitory profile, with an IC_{50} (AChE)/IC_{50} (BChE) ratio of approximately 0.54, while compound **2** showed a similar trend (SI ≈ 0.75). In contrast, compound **5** displayed a higher IC_{50} ratio of about 2.6, indicating a relative preference toward BChE over AChE within this series. The data show that the most effective cholinesterase inhibitors are those with a 4-methylcoumarin-7-arylsulfonate scaffold (Fig. 3). Furthermore, slight changes to aryl sulfonate moiety affect activity significantly. A detailed structure–activity relationship (SAR) evaluation was conducted to investigate the influence of substituents on the aromatic ring.

3.2.1 Electronic effects of *para* substituents. The *para*-substituted derivatives (**1**, **2**, **5**, and **9**) all exhibited a definite trend where the electron-donating character of these groups increased the AChE inhibition. One of the lowest IC_{50} AChE and BChE values was observed in the *p*-methoxy derivative **2** (13.075 nM and 17.325 nM). In contrast, the strong electron-withdrawing *p*-chloro analogue **5** was the least potent in the series against AChE (IC_{50} = 53.307 nM). The *p*-bromo compound **1** and the *p*-acetamido compound **9** have intermediate AChE potencies (IC_{50} = 43 312 nM and 33 000 nM). The AChE potency of *p*-acetamido (**9**), a double hydrogen-bond donor and acceptor, was found to be 33 nM, which is better than that of the halogenated analogues but still 2.5-fold weaker than *p*-OMe. In line with the observations, when a *p*-methoxy (**2**) replaces a *p*-chloro in **5**, the AChE inhibition is markedly enhanced from 53.307 nM to 13.075 nM, and the BChE inhibition is also improved (20.382 nM to 17.325 nM). On the contrary, replacing a donor group with a *p*-chloro (**5**) alternative made it less potent to AChE. The order of effect on BChE activity was not the same as for AChE, indicating that binding requirements were similar but not identical. The *p*-methoxy compound (**2**) was again very effective with a BChE IC_{50} of 17.325 nM, while the *p*-chloro compound **5** was nearly as potent against BChE (20.382 nM) despite showing the weakest performance in the AChE bioassay. Compound **5** showed 2.6-fold greater potency toward BChE than AChE, the unique selectivity pattern for this series. The *p*-bromo analogue **1** (BChE IC_{50} = 36.473 nM) was less potent than the *p*-chloro analogue against BChE. The chemical three-dimensional object (**9**) had slightly reduced activity on BChE (49.500 nM), indicating that the peripheral methoxy functional group, with which dimensionality is normally assigned to chemical structures, may not be well utilized by the BChE binding site. In summary, the *p*-OMe and *p*-Cl substituents were found to be the most effective for BChE, while *p*-Br and *p*-acetamido were less effective. The optimal *para* substituents for BChE inhibition were those with moderate hydrophobicity and possible electron-donating power (as with OMe).

3.2.2 Position and steric effects of *ortho* substituents. Substituents at the *ortho* positions of the phenylsulfonate ring had a pronounced influence on activity, generally enhancing potency for AChE and often for BChE as well. In this series, adding even a single *ortho* substituent improved AChE inhibition compared to the analogous *para*-substituted or unsubstituted systems. For example, **7** (2-chlorophenyl sulfonate) was more potent against AChE (IC_{50} = 31.500 nM) than **5** (4-chlorophenyl sulfonate, 53.307 nM). Similarly, **6** (2-methylphenyl sulfonate) showed substantially greater AChE potency (19.250 nM) than the *para*-substituted halogen analogues. The enhancement due to *ortho* substitution is dramatically illustrated by comparing the dichlorinated analog **4** (2,6-dichlorophenyl) with its mono-chlorinated counterparts: **4** inhibited AChE with IC_{50} = 28.875 nM, better than both **7** (31.500 nM, 2-Cl) and **5** (53.307 nM, 4-Cl). An even more striking case is **3**, bearing two *ortho* methyls (at positions 2 and 6) and an additional *para* methyl on the phenyl ring (a 2,4,6-trimethylphenyl or mesityl substituent). **3** was the most potent compound of the series by a considerable margin (AChE IC_{50} = 6.476 nM, BChE IC_{50} = 11.948 nM). Compared to the single *ortho* methyl compound **6** (19.250 nM for AChE IC_{50}), **3** is about 3-fold more potent. Compound **3**'s AChE IC_{50} (6.476 nM) is roughly five times lower than that of tacrine, indicating a very tight enzyme binding, likely involving both the catalytic site and peripheral site through its extended aromatic system. It is noteworthy that the nature of the *ortho* substituent (electron-donating *vs.* electron-withdrawing) modulated whether AChE or BChE was preferentially inhibited. For instance, compound **6** with an *ortho* methyl (electron-donating) showed roughly equal or slightly better potency for BChE (18.236 nM) compared to AChE (19.250 nM). In our series, the naphthalene-substituted compound **8** has a bulky polycyclic aromatic ring (naphthalene-1-sulfonate) instead of benzene. Compound **8** was a potent AChE inhibitor (IC_{50} = 27.720 nM, comparable to other monosubstituted phenyl analogues) but was the weakest BChE inhibitor of the series (IC_{50} = 53.307 nM).

3.2.3 Hydrophobicity and bulk. The SAR trends studies also underline the importance of hydrophobic bulk to the inhibition of both AChE and BChE. In most cases, potency is

Table 1 Inhibition of AChE and BChE activities by the synthesized compounds (**1–9**)

Compounds	IC_{50} (nM) AChE	R^2	IC_{50} (nM) BChE	R^2
1	43.312	0.978	36.473	0.972
2	13.075	0.984	17.325	0.978
3	6.476	0.958	11.948	0.996
4	28.875	0.989	30.130	0.985
5	53.307	0.997	20.382	0.981
6	19.250	0.993	18.236	0.999
7	31.500	0.973	46.200	0.970
8	27.720	0.995	53.307	0.981
9	33.000	0.994	49.500	0.993
Tacrine[a]	30.130	0.981	40.764	0.968

[a] Used as a positive control for AChE and BChE enzymes.

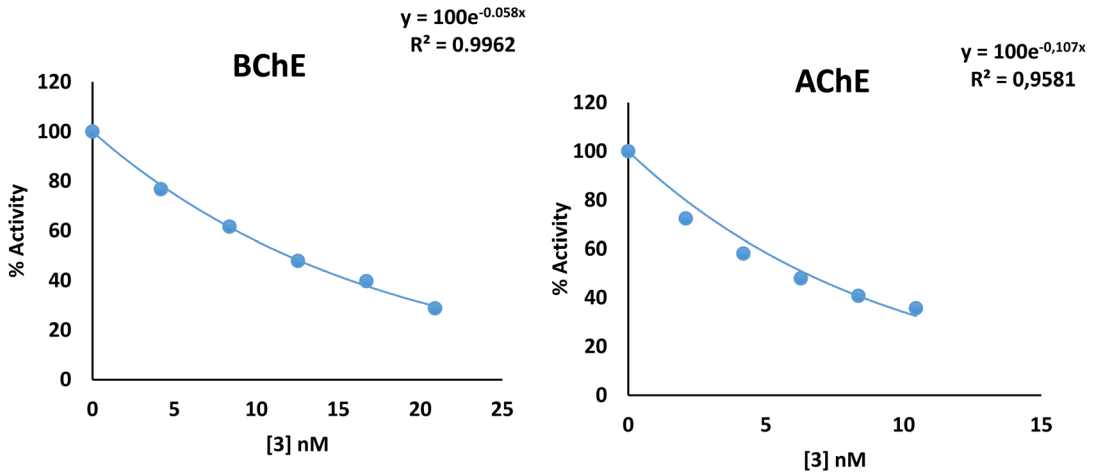

Fig. 3 IC_{50} graph of **3**, the compound with the strongest inhibitory effect for AChE and BChE.

only maximized by increasing the hydrophobic nature of the substituent to a point. The most powerful analogues (**3**, **2**, and **6**) contain large, highly hydrophobic groups (mesityl, anisole, and tolyl, respectively). Compound **3** (mesityl) showed the highest activity within the series. In contrast, compound **9**, bearing a more polar substituent (acetamido group), exhibited higher IC_{50} values compared to the more hydrophobic analogues.

3.3. Induced-fit docking study

All synthesized coumarin derivatives inhibited both AChE and BChE with low-nanomolar IC_{50} values, and several compounds outperformed the reference drug tacrine in at least one enzymatic assay, indicating a high intrinsic inhibitory potential for this chemotype. The most potent dual inhibitor among them was compound **3** (AChE IC_{50} = 6.476 nM; BChE IC_{50} = 11.948 nM), followed by compounds **2** and **6**, and compounds **5** and **8** were on the lower side of the potency range, although they also fell within the nanomolar range. This trend was used primarily as a benchmark for interpreting *in silico* outputs, rather than for quantitative correlation.

Calculations of induced-fit docking (IFD) revealed consistently favourable binding scores for all derivatives at the AChE and BChE active sites, establishing strong inhibitory profiles. The docking scores for AChE ranged from −9.423 to −14.310 kcal mol^{-1}, with **9** showing the best docking score of −14.310 kcal mol^{-1}, which is higher than tacrine (−13.337 kcal mol^{-1}), suggesting highly optimized binding inside the catalytic gorge. Compound **8** exhibits a promising profile based on its ability to occupy the gorge of BChE, which is a well-exploited feature of known anticholinesterases like tacrine (−7.370 kcal mol^{-1}). In BChE docking, the coumarin scaffold was able to adapt in a reasonable manner to the wider gorge of BChE (Table 2). The docking scores obtained in this case ranged from −8.076 to −10.632 kcal mol^{-1}, with the best score in the **8** (−10.632 kcal mol^{-1}).

Prime MM-GBSA calculations were subsequently used to refine the docking results by providing an energetic assessment of the thermodynamic stability of the protein–ligand complexes through ΔG_{bind} values. The analysis showed that compound **3** bound to both enzymes with maximum stability because it produced binding free energies that were measured at −87.29 kcal mol^{-1} for AChE and at −76.45 kcal mol^{-1} for BChE. The result showed that analog **3** produced the single best docking score because its non-bonded interaction optimization and total enthalpic effects proved to be more important than small variations that occurred during initial docking. All derivatives in the series, including **2**, **4**, **6**, and **9**, showed ΔG_{bind} values that reached dangerous levels of −70.83 to −67.57 kcal mol^{-1} for AChE, which proved that multiple compounds in the series created stable thermodynamic associations. The low docking scores, which produced highly favourable MM-GBSA energies especially for **3**, showed strong correlation with the experimentally determined inhibitory potencies, which confirmed that the proposed binding models were accurate. The two-dimensional interaction diagram of **3** in complex with AChE (Fig. 4A) illustrates a well-defined binding mode that engages both the catalytic active site (CAS) and the peripheral anionic site (PAS), a characteristic feature of effective dual-site AChE inhibitors. The aromatic coumarin core initiates various π–π stacking interactions, especially with PHE330 and TYR121, while another stacking interaction occurs between TRP84 and the aromatic moiety of the ligand. The interactions of **3** with the enzyme active site, together with their deep binding to the enzyme gorge, create strong binding stabilization through dispersive forces. The carbonyl oxygen of the coumarin ring establishes a hydrogen bond to PHE288 backbone, which functions as a central hydrogen bond for the compound. The sulfonyl oxygen atoms function as hydrogen-bond acceptors, which interact with GLY118 to strengthen binding. The combination of polar contacts together with hydrophobic interactions creates a compact interaction network that prevents ligand movement while maintaining the attached state. The arrangement of polar groups outside the deep hydrophobic areas reduces desolvation costs, which explains the highly positive ΔG_{bind} result predicted for **3** in AChE. The

Table 2 Summary of induced-fit docking scores and prime/MM-GBSA-derived binding free energies for highly active coumarin-based enzyme inhibitors

Compound	AChE		BChE	
	IFD docking score (kcal mol^{-1})	MM-GBSA ΔG_{bind} (kcal mol^{-1})	IFD docking score (kcal mol^{-1})	MM-GBSA ΔG_{bind} (kcal mol^{-1})
1	−9.423	−61.51	−8.076	−59.42
2	−10.287	−70.83	−9.212	−63.14
3	−9.874	−87.29	−8.832	−76.45
4	−9.843	−65.57	−8.959	−61.77
5	−9.642	−49.34	−8.380	−65.82
6	−9.458	−65.62	−8.926	−69.25
7	−9.937	−60.75	−9.445	−58.62
8	−11.024	−60.13	−10.632	−53.06
9	−14.310	−67.57	−10.137	−53.00
Tacrine	−13.337	−70.54	−7.370	−58.97

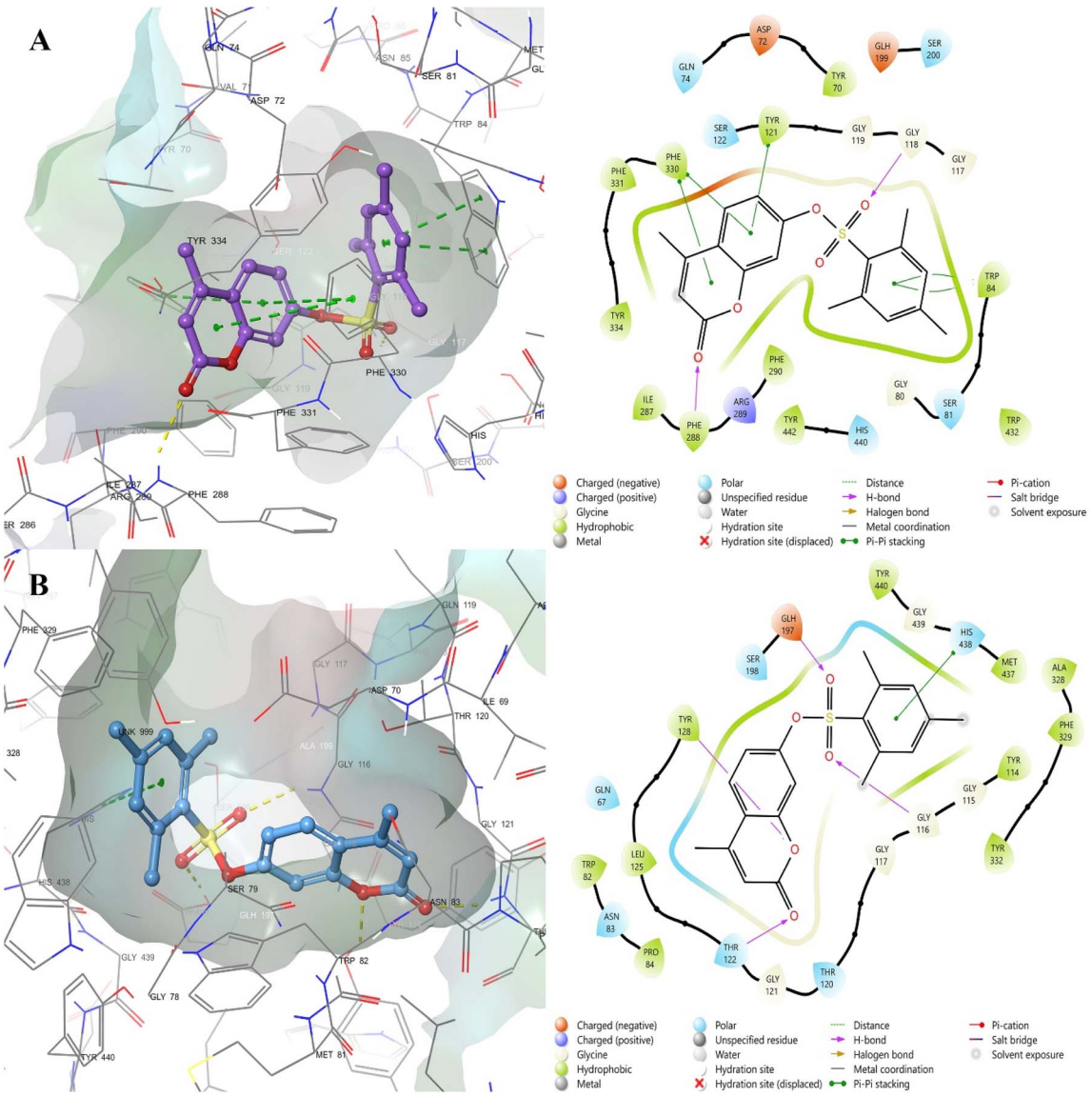

Fig. 4 Three-dimensional docking conformations of compound **3** in AChE (A) and BChE (B) (left panels) with the corresponding two-dimensional ligand–receptor interaction diagrams (right panels).

binding mode shown in Fig. 4A explains the strong predicted affinity of **3** together with its high experimental inhibition results.

The BChE active site shows a two-dimensional interaction pattern that identifies three elements that match the crucial characteristics of AChE but simultaneously demonstrates the changes made to accommodate the BChE gorge, which exhibits both greater size and higher flexibility. The coumarin ring system again establishes hydrogen-bonding interactions with residues of the catalytic pocket, notably THR122 and TYR128. The sulfonyl oxygen atoms function as hydrogen-bond acceptors, which allow binding to GLY116 and GLH197, thus providing added support to the central scaffold structure. The active-site cavity contains hydrogen-bonding and hydrophobic interactions, which extend throughout its space because BChE has a larger active-site structure, which explains the less negative yet still highly favorable ΔG_{bind} value of −76.45 kcal mol^{-1}.

The active-site residue HIS438 and **3** maintain π–π stacking interactions, which display reduced stacking interactions or more distant stacking interactions than those found in the AChE complex. The experimental and calculated affinity values for **3** show decreased binding to BChE when compared to AChE. The BChE binding cavity shows efficient complementarity with the coumarin scaffold because the two components maintain stable polar contacts while creating an extensive hydrophobic enclosure. The upper gorge region of the ligand shows that substituents point toward this area, which enables **3** to reach both catalytic and peripheral BChE sites that help regulate cholinesterase activity in neurodegenerative diseases.

3.4. MD simulations

The 250 ns molecular dynamics (MD) trajectories of the **3**-AChE and **3**-BChE complexes confirm that the docked poses are induced by docking and not by static modelling. The molecular interaction fingerprints generated from the two-dimensional (2D) ligand–enzyme interaction maps (Fig. 5a and 6a) display dissimilar yet complementary binding conformations of the compound **3** within AChE and compound **3** within BChE, respectively, which are due to the structural and physicochemical differences between the two cholinesterases. In the **3**-AChE complex, noticeable hydrogen bonding and aromatic interactions can be seen in the ligand interaction network. The sulfonyl moiety directly or rather through a water molecule establishes persistent hydrogen bonds with ASP72, SER81, and ASN85, residues close to the catalytic anionic site (CAS), thereby playing a central anchoring role. It is known that π–π stacking interaction with TYR334, a key residue lining the aromatic gorge of AChE, plays a significant role in ligand stabilization. More hydrophobic interactions with PHE331, PHE330, and TRP84 stabilize the position of the ligand in the active gorge of the enzyme, and the **3** binds well to the CAS and peripheral aromatic sites. The presence of water bridges at high occupancies suggests a solvent-assisted stabilization mechanism, typically for high-affinity AChE inhibitors. In contrast, the **3**-BChE complex may have a binding profile that is mainly determined by hydrogen bond formation and hydrophobic enclosure, in keeping with the broader and more flexible BChE active site. The ligand forms highly persistent hydrogen bonds with GLY116, THR122, TYR128, and GLU197, with interaction occupancies exceeding 85–90%. The aromatic centre of **3** also engages in π–π interaction with TRP82, a residue critical for substrate recognition in BChE. In contrast to the AChE complex, interactions mediated by water are less significant, suggesting that **3** stabilizes mainly through contact with the enzyme. The pattern of interactions illustrates a tighter and more specific adaptation of **3** to the BChE binding pocket. The root mean square deviation (RMSD) profiles (Fig. 5b and 6b) show the overall stability of both the enzyme–ligand complexes during 250 ns of molecular dynamics simulations. In the case of the **3**-AChE system, the RMSD of the protein backbone becomes stabilized at about 1.2–1.5 Å after the initial equilibration. This showed that the enzyme has remained structurally stable throughout the simulation. RMSD values of the ligand (protein fitted) vary from 0.6 to 1.0 Å, indicating a moderate conformational flexibility, but remain firmly fused at the active site. The RMSD for ligand-fitted systems shows internal rearrangements

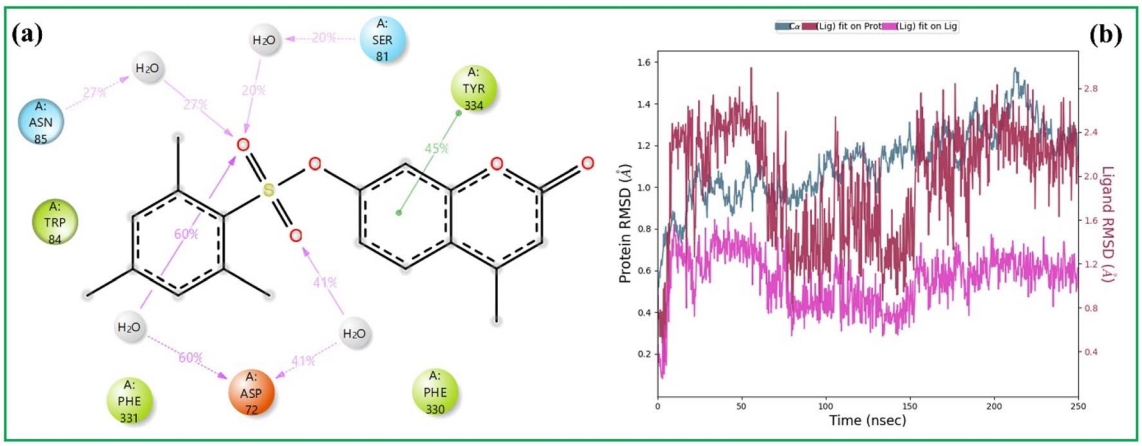

Fig. 5 250 ns molecular dynamics analysis of the **3**-AChE complex. (a) Representative two-dimensional ligand–protein interaction map and (b) RMSD profiles of protein Cα atoms (light blue).

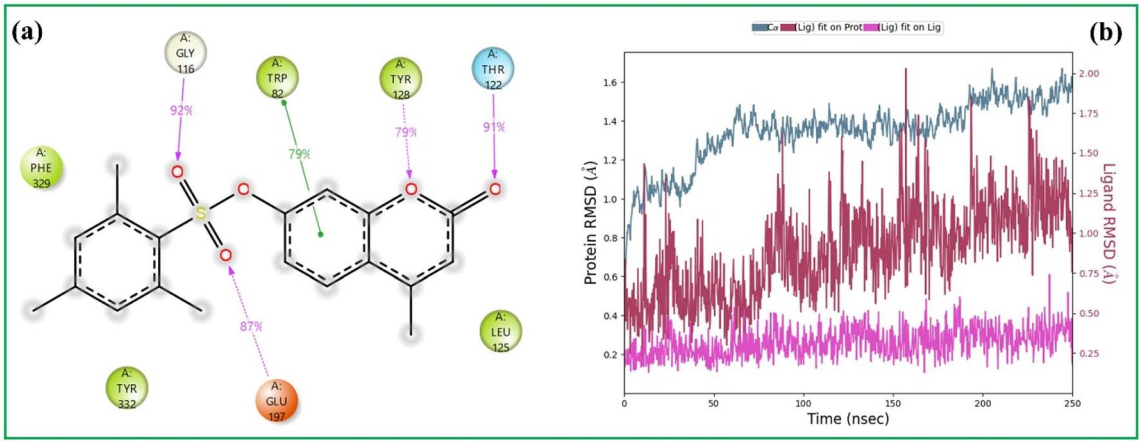

Fig. 6 250 ns molecular dynamics analysis of the **3**-BChE complex. (a) Representative two-dimensional ligand–protein interaction map and (b) RMSD profiles of protein Cα atoms (light blue).

of the ligand are minimal, and there is a well-defined and stable binding mode. The protein RMSD values for the **3**-BChE complex are slightly greater than those of AChE and stabilize at about 1.4–1.6 Å. The observation is expected since BChE is more flexible than AChE. The ligand RMSD is remarkably below 0.5 Å for most of the simulation, indicating that the ligand, once bound, is immensely stable. **3** displays few positional adjustments in the BChE active site as a result of fitting well into the site. The root mean square fluctuation (RMSF) analysis for the Cα atoms (Fig. 1c and 2c in SI file) will show local flexibility changes due to ligands. Most of the residues in the **3**-AChE complex possess an RMSF value less than 1.0 Å, indicating overall rigidity. Fluctuations in the loops located far away from the binding site are slightly increased, whereas the residues directly involved in ligand binding, *e.g.*, RP84, ASP72, SER81, and PHE330, are remarkably rigid. According to the analysis, stabilization of key catalytic and aromatic gorge residues suggests that **3** appears to reduce local flexibility and substrate access and turnover. The **3**-BChE system has a similar overall RMSF pattern to the coumarin sulfonates-AChE and -BChE systems, but with moderately higher fluctuations in more peripheral regions. This is again consistent with the intrinsic flexibility of BChE. Notably, the reduced mobility of residues that form strong hydrogen bonds with **3** (GLY116, THR122, TYR128, and GLU197) indicates that ligand binding stabilizes the architecture of the active site. The RMSF profiles of the ligand (Fig. 1d and 2d in the SI file) further depict the dynamics of compound **3** in the binding pockets. Compound **3** has large excitations at the terminal aromatic and substituent atoms, especially for the atoms not attached through strong interactions. On the other hand, the atoms pertaining to the sulfonyl linker and the central aromatic backbone display very low RMSF values of ~0.6–0.8 Å. Thus, they act as structural anchors in the AChE. The overall ligand RMSF values for **3** were lower, mostly <0.7 Å, indicating that it has a more rigid binding conformation. There is low flexibility at peripheral substituents, while the stability of aromatic core and hydrogen-bonding functionalities is high. The low ligand RMSD of the BChE complex may likely be due to its rigidity. The interaction fraction histograms (Fig. 1e in the SI file) present a quantitative summary of the stability and frequency of the ligand-residue contacts during the simulation. The amino acids of the **3**-AChE complex, like ASP72, TRP84, PHE330, and TYR334, show high interaction fractions, which are equally contributed by H-bond, hydrophobic, and water bridge. **3** binds through multiple modes and has a longer residence time in the AChE gorge due to its characteristics. The complex **3**-BChE has large interaction fractions for the amino acids TRP82, GLY116, THR122, TYR128, and GLU197. The respective interactions occur *via* hydrogen docking, hydrophobic, and other interactions. The fact that these interactions do not disappear during the entire trajectory indicates a strong and stable binding mode, along with low ligand flexibility. So overall, molecular dynamics results indicate that **3** is quite suitable for AChE inhibition and that the stabilization of **3** complex in the narrow aromatic gorge results from aromatic stacking and solvent-assisted hydrogen bonding. The BChE active site shows better stability and interaction duration for **3** because its larger active site cavities enable direct hydrogen bonds and hydrophobic protection. The results show that even small changes in ligand and enzyme active site structure lead to different dynamic behavior, which explains why AChE and BChE select different substrates. The combination of RMSD and RMSF and interaction analyses demonstrates strong evidence that proves compound **3** maintains stability while inhibiting AChE and BChE and shows potential as a cholinesterase-targeted therapeutic candidate.

3.5. ADME and drug-likeness profile

In silico ADME predictions suggest that the coumarin derivatives possess a generally favorable drug-like profile and are suitable for central nervous system (CNS) applications. All compounds comply with Lipinski's rule of five and rule of three, with zero violations, indicating an appropriate balance of molecular weight, lipophilicity, hydrogen-bond donors/acceptors, and polarity. The molecular weights range from approximately 330 to 395 Da, with no hydrogen-bond donors

Table 3 Predicted ADME (absorption, distribution, metabolism, and excretion) properties of the coumarin derivative compounds

Compound	mol MW	donorHB	acceptHB	QP log *Po*/w	QP log *S*	QP log HERG	QPPCaco	QP log BB	QPPMDCK	Percent human oral absorption	Rule of five	Rule of three
1	395.224	0.000	7.000	2.037	−3.577	−5.826	416.621	−0.867	509.059	85.760	0	0
2	346.354	0.000	7.750	1.466	−2.537	−5.526	499.609	−0.986	233.956	83.831	0	0
3	358.408	0.000	7.000	2.257	−3.620	−5.208	623.662	−0.837	296.971	90.187	0	0
4	385.218	0.000	7.000	2.261	−3.698	−5.369	438.959	−0.680	986.029	87.476	0	0
5	350.773	0.000	7.000	1.964	−3.256	−5.607	499.621	−0.756	576.628	86.744	0	0
6	330.355	0.000	7.000	1.681	−2.803	−5.492	533.505	−0.873	251.947	85.596	0	0
7	350.773	0.000	7.000	1.783	−2.912	−5.522	500.697	−0.790	416.500	85.704	0	0
8	366.388	0.000	7.000	2.446	−3.805	−6.363	499.894	−0.971	234.098	89.571	0	0
9	373.380	1.000	9.500	1.174	−3.545	−5.938	138.705	−1.677	58.486	72.158	0	0

and 7–9.5 acceptors, which together support good membrane permeability while preserving sufficient polar surface for solubility and target recognition.

Predicted human oral absorption values are high for most derivatives, typically above 83%, with particularly favorable values for **3** (90.187%) and **8** (89.571%), while only **9** (72.158%) falls into the lower, yet still acceptable, absorption range. The QPPCaco and QPPMDCK values indicate that the compounds possess favorable intestinal permeability, suggesting good potential for oral absorption, while maintaining an acceptable permeability profile overall. The Caco-2 permeability of **3** and **6** demonstrates exceptionally high values through their permeability measurements of 623.662 and 533.505, which confirm their optimized log *P* measurements of 2.257 to 1.681. The predicted QPlogBB values typically range from −1.0 to 0.3 for compounds with the potential to cross the blood–brain barrier, whereas values below −1.0 are generally associated with poor brain penetration. In the present study, the QPlogBB values of the investigated compounds (−0.68 to −1.68) suggest limited to moderate BBB permeability overall. Notably, compound **3** (QP log BB = −0.837) falls within the intermediate range, indicating a relatively favorable balance for blood–brain barrier penetration and a potential to reach the central nervous system. The QPlogHERG values stay within boundaries, which shows that hERG channel blockade does not present an acute threat, which decreases cardiotoxicity risks when compared to traditional cholinesterase inhibitors. The combination of ADME descriptors together with strong and stable binding to AChE and BChE makes **3** and its coumarin derivatives promising candidates for lead development, which will undergo further improvement and testing in Alzheimer's disease research (Table 3).

4. Conclusions

In this study, a series of novel coumarin-based sulfonate esters (**1–9**) was successfully synthesized starting from 4-methyl-7-hydroxycoumarin *via* Pechmann condensation, followed by sulfonylation with various aryl sulfonyl chlorides. The synthesized compounds were characterized by IR and NMR spectroscopy, along with their physical properties. Biological evaluation revealed that all compounds exhibited significant inhibitory activity against AChE and BChE, with IC_{50} values in the low-nanomolar range. Among them, compound **3** emerged as the most potent dual inhibitor (IC_{50} = 6.476 nM for AChE and 11.948 nM for BChE). SAR analysis indicated that the electronic properties, steric size, and positional orientation of substituents on the phenyl ring influence inhibitory potency. Computational studies provided supportive insights into ligand–enzyme interactions. Induced-fit docking suggested favorable binding orientations within the enzyme gorge, while MM-GBSA calculations and molecular dynamics simulations indicated stable ligand–enzyme complexes over time. In addition, *in silico* ADME analysis predicted favorable pharmacokinetic properties for the synthesized compounds, including compliance with Lipinski's rule of five and acceptable blood–brain barrier penetration, with no significant predicted cardiotoxicity risk. Hence, the combined synthetic, biological, and computational findings identify coumarin-based arylsulfonate derivatives as a promising scaffold for cholinesterase inhibition. In particular, compound **3** represents a valuable lead for further structural optimization and future investigations.

Author contributions

Ehsan Ullah Mughal: conceptualization, supervision, validation, investigation, resources, data curation, writing – original draft, writing – review & editing, visualization, project administration, funding acquisition. Nafeesa Naeem: data collection, visualization, validation, formal analysis, investigation, writing – original draft, writing – review & editing. Aneela Shaheen Cheema: experimental work performance. Gehan Ahmed Othman: FTIR analysis, formal analysis, investigation. Amina Sadiq: formal analysis, investigation. Songül Bayrak: biological and computational studies, writing – original draft. Namık Kılınç: biological and computational studies, writing – original draft. Mohammed B. Hawsawi: NMR analysis. SM Gomha: formal analysis, investigation. Züleyha Almaz: biological and computational studies, writing – original draft.

Conflicts of interest

Authors have no conflicts of interest to declare.

Data availability

All the data is provided in the manuscript and supplementary information (SI). Supplementary information is available. See DOI: https://doi.org/10.1039/d6ra02535h.

Acknowledgements

The authors extend their appreciation to the Deanship of Research and Graduate Studies at King Khalid University for funding this work through Large Research Project under grant number RGP2/370/46.

References

1 Z. F. Vahid, M. Eskandani, H. Dadashi, S. Vandghanooni and M.-R. Rashidi, *Heliyon*, 2024, **10**, 1–22.
2 E. Polo, L. Prent-Peñaloza, Y. A. R. Núñez, L. Valdés-Salas, J. Trilleras, J. Ramos, J. A. Henao, A. Galdámez, A. Morales-Bayuelo and M. Gutiérrez, *J. Mol. Struct.*, 2021, **1224**, 129307.
3 Q. Q. Lu, Y. M. Chen, H. R. Liu, J. Y. Yan, P. W. Cui, Q. F. Zhang, X. H. Gao, X. Feng and Y. Z. Liu, *Drug Dev. Res.*, 2020, **81**, 1037–1047.
4 M. Bortolami, D. Rocco, A. Messore, R. Di Santo, R. Costi, V. N. Madia, L. Scipione and F. Pandolfi, *Expert Opin. Ther. Pat.*, 2021, **31**, 399–420.
5 A. Contestabile, *Behav. Brain Res.*, 2011, **221**, 334–340.
6 J.-L. Wang, X.-Y. Sha, Y. Shao, Z.-H. Zhang, S.-M. Huang, H. Lin, S.-Y. Gan, N. Zhang, X.-Y. Xia and Y.-N. Sun, *Cell*, 2026, **189**, 640–658.
7 T. L. Rosenberry, X. Brazzolotto, I. R. Macdonald, M. Wandhammer, M. Trovaslet-Leroy, S. Darvesh and F. Nachon, *Molecules*, 2017, **22**, 2098.
8 S. Kang, Q. Wu, J. Shen and C. Wu, *Sci. Rep.*, 2024, **14**, 23742.
9 Q. Yan, Q. Qin, S. Zhang, F. Chen, Y. Ru, Y. Zhong and G. Wu, *Crit. Rev. Food Sci. Nutr.*, 2026, **66**, 2335–2351.
10 B. Brus, U. Kosak, S. Turk, A. Pislar, N. Coquelle, J. Kos, J. Stojan, J.-P. Colletier and S. Gobec, *J. Med. Chem.*, 2014, **57**, 8167–8179.
11 Z. Yan, B. Yu, X. Lan, X. Cui, D. Zhao, L. Qiu, H. Wang, W. Wang, L. Chen and L. Jin, *J. Mol. Struct.*, 2024, **1308**, 138331.
12 N. Sultana, M. Sarfraz, S. T. Tanoli, M. S. Akram, A. Sadiq, U. Rashid and M. I. Tariq, *Bioorg. Chem.*, 2017, **72**, 256–267.
13 Z. Almaz, A. Oztekin, A. Tan and H. Ozdemir, *J. Mol. Struct.*, 2021, **1244**, 130918.
14 Z. Hui, W. Lai-Fa, W. Xue-Qin, D. Ling, H. Bin-Sheng and J.-M. Li, *J. Asian Nat. Prod. Res.*, 2024, **26**, 1405–1420.
15 F. S. Tokalı, *Future Med. Chem.*, 2025, **17**, 1071–1091.
16 H. Luo, Y. Xiang, X. Qu, H. Liu, C. Liu, G. Li, L. Han and X. Qin, *Front. Pharmacol.*, 2019, **10**, 395.
17 S. Zhang, Z. Wu, S. Zhang, Y. Ru, Q. Wang, H. Tong, Q. Qin, Q. Yan, Z. Li and G. Wu, *Food Funct.*, 2025, 8320–8344.
18 U. Farooq, M. Islam, Z. Batool, S. N. Mali, R. D. Jawarkar, S. S. Gurav, R. D. Alharthy, H. Şenol, N. Sadeghian and P. Taslimi, *Arch. Pharmazie*, 2025, **358**, e70050.
19 A. F. Kassem, M. A. Omar, A. Temirak, R. A. El-Shiekh and A. M. Srour, *Future Med. Chem.*, 2024, **16**, 1615–1631.
20 R. Saeed, H. Z. Tariq, A. Althobaiti, N. Sadeghian, P. Taslimi, M. Al-Rashida, T. Islam, H. K. Thabet, H. Aftab and H. Şenol, *Sci. Rep.*, 2025, 1–19.
21 Ü. Yaşar, Y. Demir, İ. Gönül, M. S. Özaslan, G. G. Çelik, C. Türkeş and Ş. Beydemir, *Chem. Biodiversity*, 2025, **22**, e202402893.
22 M. A. Omar, R. A. El-Shiekh, D. H. Dawood, A. Temirak and A. M. Srour, *Future Med. Chem.*, 2023, **15**, 2269–2287.
23 A. Pourparizi, H. Nadri, N. Naghsh, A. R. Eider and F. Pourrajab, *J. Mol. Struct.*, 2023, **1294**, 136334.
24 E. Hu, Z. Li, T. Li, X. Yang, R. Ding, H. Jiang, H. Su, M. Cheng, Z. Yu and H. Li, *Chin. Med.*, 2023, **18**, 40.
25 C. Zhou, Z. Yu, T. Chen, Q. Chen, Y. Zhang, J. Cai, C. Xu and L. Yu, *Phytomedicine*, 2025, 157548.
26 L. G. de Souza, M. N. Rennó and J. D. Figueroa-Villar, *Chem. Biol. Interact.*, 2016, **254**, 11–23.
27 M. Erdoğan, A. Onder, Y. Demir and F. Comert Onder, *ACS Omega*, 2024, **9**, 46860–46878.
28 A. Korkmaz, *J. Inst. Sci. Technol.*, 2022, **12**, 918–932.
29 M. I. El-Gamal and C.-H. Oh, *Eur. J. Med. Chem.*, 2014, **84**, 68–76.
30 S. Bai, R. Wu, S. Wan, L. Chen, X. Lv, Y. Xiao, F. Wang, X. Wei and M. Li, *Russ. J. Gen. Chem.*, 2025, **95**, 1464–1475.
31 U. Salar, K. M. Khan, J. Iqbal, S. A. Ejaz, A. Hameed, M. Al-Rashida, S. Perveen and M. N. Tahir, *Eur. J. Med. Chem.*, 2017, **131**, 29–47.
32 H.-L. Jang, M. I. El-Gamal, H.-E. Choi, H.-Y. Choi, K.-T. Lee and C.-H. Oh, *Bioorg. Med. Chem. Lett.*, 2014, **24**, 571–575.
33 Y. Hu, Y. Shen, X. Wu, X. Tu and G.-X. Wang, *Eur. J. Med. Chem.*, 2018, **143**, 958–969.
34 G. L. Ellman, K. D. Courtney, V. Andres Jr and R. M. Featherstone, *Biochem. Pharmacol.*, 1961, **7**, 88–95.
35 S. Bayrak, S. Gerni, C. Ozturk, B. Bakan, S. Elmas and A. Aliyeva, *Food Biophys.*, 2025, **20**, 148.
36 Z. Almaz, *J. Biochem. Mol. Toxicol.*, 2023, **37**, e23277.
37 A. Tan and Z. Almaz, *J. Mol. Struct.*, 2023, **1277**, 134854.
38 A. Tan and Z. Almaz, *J. Iran. Chem. Soc.*, 2022, **19**, 2833–2844.
39 B. Kuzu and Y. Demir, *Arch. Biochem. Biophys.*, 2025, 110504.
40 W. Sherman, T. Day, M. P. Jacobson, R. A. Friesner and R. Farid, *J. Med. Chem.*, 2006, **49**, 534–553.
41 A. Akıncıoğlu, S. Göksu, A. Naderi, H. Akıncıoğlu, N. Kılınç and İ. Gülçin, *Comput. Biol. Chem.*, 2021, **94**, 107565.
42 N. Gök, A. Akıncıoğlu, E. Erümit Binici, H. Akıncıoğlu, N. Kılınç and S. Göksu, *Arch. Pharmazie*, 2021, **354**, 2000496.
43 N. Kılınç, U. Güller and Z. Alım, *Russ. J. Bioorg. Chem.*, 2022, **48**, 720–730.
44 Z. Alım, H. Şirinzade, N. Kılınç, E. Dilek and S. Süzen, *J. Mol. Struct.*, 2024, **1311**, 138276.
45 F. S. Tokalı, H. Şenol, Ş. Ateşoğlu, P. Tokalı and F. Akbaş, *J. Mol. Struct.*, 2025, **1319**, 139519.
46 H. Şenol, *ChemistrySelect*, 2024, **9**, e202303927.
47 Z. Köksal and H. Şenol, *Arch. Pharmazie*, 2025, **358**, e2400909.

48 C. Öztürk, S. Bayrak, S. Gerni, Z. Almaz, N. Kılınç, H. Özdemir and U. Atmaca, *ChemistrySelect*, 2026, **11**, e04032.
49 G. Madhavi Sastry, M. Adzhigirey, T. Day, R. Annabhimoju and W. Sherman, *J. Comput. Aided Mol. Des.*, 2013, **27**, 221–234.
50 S. Genheden and U. Ryde, *Expert Opin. Drug Discov.*, 2015, **10**, 449–461.
51 B. Zengin Kurt, D. Öztürk Civelek, E. B. Cakmak, Y. Kolcuoğlu, H. Şenol, B. m. N. Sağlık Özkan, A. Dag and K. Benkli, *J. Med. Chem.*, 2024, **67**, 4463–4482.
52 S. A. Adcock and J. A. McCammon, *Chem. Rev.*, 2006, **106**, 1589–1615.